

Tracing Early Cosmic Chemical Enrichment: A Uniform XMM-Newton Survey of Metallicity in Galaxy Groups and Clusters

ANNE E. BLACKWELL ¹, JOEL N. BREGMAN ¹ AND SOPHIA CHAN DAVIS ²

¹University of Michigan, Ann Arbor, MI 48104, USA

²University of Texas at San Antonio, San Antonio, TX 78249, USA

(Received 2025 September 23; Revised 2025 November 19; Accepted 2025 November 20)

ABSTRACT

Observed metal abundances in the intracluster medium (ICM) of galaxy groups and clusters, Z_{ICM} , exceed what is expected from present-day stellar populations alone. Galaxy clusters are presumed to be near closed-box systems, allowing constraints to be placed on the origins of metals and stellar populations responsible for Z_{ICM} . We present a uniform XMM-Newton survey of 26 galaxy groups and clusters, measuring radial metallicity profiles and relating Z_{ICM} with the stellar fraction M_*/M_{gas} . We determine Z_{ICM} via spectral fitting across multiple annuli finding a best fit of $Z_{ICM} = -0.08_{-0.07}^{+0.07} \log\left(\frac{M_*}{M_{gas}}\right) + 0.30_{-0.06}^{+0.06}$ with intrinsic scatter $\sigma_p = 0.09_{-0.01}^{+0.02}$. We use closed-box chemical evolution models to estimate the metallicity yield from observable stellar populations, incorporating updated supernova yields and corrections for metals locked in remnants, $Z_* = (1.14 \pm 0.52) \log\left(1 + \frac{M_*}{M_{gas}}\right)$. Our results demonstrate that present-day stellar populations systematically underpredict Z_{ICM} , with an inferred excess component increasing in systems with low M_*/M_{gas} . This trend supports the need for an early enrichment population (EEP) distinct from visible stars, Z_{EEP} . We find this necessity holds when reconsidering the closed-box assumption by removing all galaxy groups, potential leaky systems, deriving Z_{EEP} within 1σ when including and excluding groups. Three systems (NGC1132, NGC5098, and NGC4325) deviate from the survey trend, exhibiting steep negative radial metallicity gradients and unusually low Z_{ICM} . We posit these systems to be late-forming whose ICM enrichment reflects only recent stellar populations. Our analysis quantifies the necessity of an EEP and provides trends for testing cluster chemical evolution models.

Keywords: galaxies: clusters: intracluster medium — stars: Population II — supernovae: general — X-rays: galaxies: clusters

1. INTRODUCTION

Metals serve as vital tracers of stellar evolution, feedback processes, and the integrated history of star formation throughout the Universe. In particular, the intracluster medium (ICM) of galaxy clusters is a critical environment for studying cosmic chemical enrichment (e.g., Baldi et al. 2012; Mantz et al. 2017; Mernier et al. 2017; Ghizzardi et al. 2020; Lovisari et al. 2020; Gatuzz et al. 2023a,b). Galaxy clusters possess deep potential wells that retain enriched material, making them ideal laboratories for tracing the production of metals over cosmic time.

Chemical enrichment models often adopt a “closed-box” framework, in which gas and metals are neither lost nor gained from the system. The observed ICM metallicity, Z_{ICM} , should be fully accounted for by the met-

als produced by the current observable stellar populations, Z_* , under an assumed initial mass function (IMF) within this model. However, a growing body of evidence suggests that this assumption may not adequately describe the observed metallicity trends, particularly in systems with low stellar mass fractions, M_*/M_{gas} (Bregman et al. 2010; Blackwell et al. 2022; Blackwell & Bregman 2025). Prior works indicate that closed-box models systematically underpredict Z_{ICM} , implying that an additional stellar population may have contributed significantly to an early enrichment, the early enrichment population (EEP) (Elbaz et al. 1995; Loewenstein 2001; Bregman et al. 2010; Loewenstein 2013; Renzini & Andreon 2014; Blackwell et al. 2022; Blackwell & Bregman 2025).

Several alternative theories have been proposed to resolve this discrepancy. Zibetti et al. (2005) suggested that the missing stellar population may be found in diffuse intracluster light (ICL), but subsequent observations showed that the ICL does not contain enough mass to account for excess metals. Renzini & Andreon (2014) provide a comprehensive review of the broader metal budget problem and outline various scenarios that could explain the enrichment, including hierarchical assembly and selective metal loss. More recently, Biffi et al. (2025) used cosmological simulations to model the origin of metals in galaxy groups and clusters. They find that the stellar populations within their simulations accurately recreate Z_{ICM} and therefore claim to alleviate the iron budget tension. However, they overpredict the stellar mass and consequently the iron locked in stars, therefore underpredicting the iron share, the ratio of Fe diffused in the ICM to that locked in stars, (Renzini & Andreon 2014; Ghizzardi et al. 2020) by approximately an order of magnitude compared to observations. Despite these efforts and tensions, the challenge first identified by Elbaz et al. (1995) remains unresolved, and the EEP hypothesis has not yet been conclusively ruled out.

Previous efforts to constrain the EEP include the works of Blackwell et al. (2022) and Blackwell & Bregman (2025), who analyzed trends in Z_{ICM} as a function of M_*/M_{gas} . In particular, Blackwell & Bregman (2025), hereafter B25, conducted a uniform analysis of archival XMM-Newton data for 26 galaxy groups and clusters with $M_{*,500}$ and $M_{gas,500}$ from Laganá et al. (2013). They derived plausible IMFs for the EEP that could account for the observed deviations from closed-box predictions.

In this study, we present the full dataset and X-ray spectral fit results for the 26 galaxy groups and clusters comprising the survey. We evaluate the trend of Z_{ICM} vs M_*/M_{gas} under a closed-box chemical evolution model and demonstrate the need for an early enrichment component. We derive the expected contribution from present-day stellar populations, Z_* , using updated yields from Type Ia and core-collapse supernovae and accounting for metals locked in stellar remnants. This methodology builds upon that introduced by Loewenstein (2013), incorporating more recent estimates of supernova rates, IMF variations, and additional consideration of metals locked in remnants.

The residual metallicity, $Z_{EEP} = Z_{ICM} - Z_*$, is the necessary contribution from the theorized EEP required to reproduce observations of Z_{ICM} . The contribution of Z_{EEP} may vary across systems as it may be entangled with other cluster properties such as entropy profiles, cuspsiness, or dynamical history. We investigate the de-

pendence of Z_{EEP} on these properties in a companion study (Gherri et al., in prep).

For this paper, we assume a Λ CDM cosmology with $H_0 = 70 \text{ km s}^{-1} \text{ Mpc}^{-1}$, a baryon density parameter of $\Omega_b = 0.046$, dark matter density parameter of $\Omega_{DM} = 0.24$, and the total baryon density parameter is $\Omega_m = 0.29$ (Planck Collaboration et al. 2018). We also adopt a Kroupa-Salpeter IMF as developed by Bell et al. (2003) and adopted in Blackwell et al. (2022) and B25. This IMF has a slope of $\alpha = 0.35$ in the mass range $0.5 - 1M_\odot$, and a slope of $\alpha = 1.35$ in the mass range $1 - 150M_\odot$ for an IMF defined as $\phi(m) = m^{-(1+\alpha)}$ (per unit log mass).

This paper is organized as follows. In Section 2, we describe the survey selection, data reduction, and spectral analysis methodology. Section 3 presents the fit to the observed Z_{ICM} vs M_*/M_{gas} relation and the derivation of Z_* and Z_{EEP} . In Section 4, we discuss the implications of our findings, including assumptions, systematics, and the role of outlier systems. We conclude in Section 5.

2. SURVEY DATA REDUCTION AND ANALYSIS

Our sample of 26 galaxy groups and clusters follows from B25, a subset of galaxy groups and clusters identified in Laganá et al. (2013). Each system has uniformly derived $M_{*,500}$ and $M_{gas,500}$, using the critical overdensity, and sufficient archival XMM Newton data to determine Z_{ICM} to approximately 10% precision.

We adopt R_{500} values from Laganá et al. (2013), which were derived for galaxy groups in that work and for galaxy clusters in Maughan et al. (2008). In Maughan et al. (2008), R_{500} was determined iteratively using the $Y_X - M_{500}$ scaling relation determined by Vikhlinin et al. (2006) (Kravtsov et al. 2006). The iterative process involved measuring the plasma temperature and the gas mass within the region $0.15 - 1R_{500}$ until R_{500} converged within 1%. For galaxy groups, Laganá et al. (2013) computed R_{500} using their Equation 6 from Lima Neto et al. (2003), assuming an isothermal temperature profile measured within 300 kpc.

Our sample inherits the selection criteria of Laganá et al. (2013) who combined nine galaxy groups and 114 clusters spanning $0.02 < z < 1.3$ and $M_{500} \sim 10^{13} - 4 \times 10^{15} M_\odot$. Of those, 36 systems had sufficient optical and X-ray data to determine stellar and gas masses out to R_{500} . This sample is X-ray luminosity limited to $L_X = 1.9 \times 10^{43} \text{ erg/s}$. This criterion inherently favors X-ray bright, gas-rich systems, excluding low-mass or gas-poor groups with insufficient X-ray observations. That is, the systems we chose for this study favor high signal-to-noise observations. Prioritizing observation quality ensures reliable measurements of Z_{ICM} , M_*

and M_{gas} , but at the cost of reduced sample completeness. Our sample selection emphasizes measurement precision over full representation of the M_*/M_{gas} range. These excluded systems would likely populate the high end of the M_*/M_{gas} distribution, potentially biasing our sample. We do not explicitly correct for this sample incompleteness within our modeling. The derived trends therefore should only be interpreted for X-ray luminous systems within $0.039 < M_*/M_{gas} < 0.48$.

The final sample consideration is the contribution from non-thermal pressure. Values adopted from Maughan et al. (2008) and Laganá et al. (2013) either do not, or very briefly touch on the contribution from non-thermal pressure, and only in the galaxy group regime. Simulations find that non-thermal pressure may contribute $\sim 10\%$ of the total pressure support for relaxed galaxy clusters (Lau et al. 2009). This is a very small contribution, and likely encapsulated in the errors of M_* and M_{gas} as the errors are $\sim 30\%$ and $\sim 7\%$ on average, respectively. We do not consider any corrections from non-thermal pressure in this survey.

2.1. XMM-Newton Data Reduction and Analysis

We followed the same data reduction and analysis outlined in Blackwell et al. (2022) which follow from Snowden et al. (2008), using the XMM-ESAS Cookbook, and the Extended Source Analysis Software. We used SAS version (19.1.0)¹, and CALDB (version 4.9.3)². We examined each light curve to ensure proper exclusion of flare intervals, and used *emanom* to check for anomalous chips which were then excluded from the spectral extractions.

We extracted spectra from five radial bins defined as $< 0.1R_{500}$, $0.1 - 0.21R_{500}$, $0.21 - 0.39R_{500}$, $0.39 - 0.53R_{500}$, and $0.53 - 0.7R_{500}$. These are the same regions as B25. The value R_{500} is defined as the radius at which the average cluster density is 500 times that of the Universe at the cluster redshift.

We accounted for two known chip phenomena during spectral extraction: the point-spread function and PN-chip counting of X-ray photons. The point-spread function was considered by generating crossarfs which redistribute the X-ray photons into the most probable annuli they physically originated. We used *evselect* and *arfgen* to generate additional ARF files to account for the crossarf. For the PN chip, we extracted two spectra using PATTERN=0 for a low-energy spectrum (0.6-2 keV), and PATTERN=4 for a high-energy spectrum (1.0-7.0 keV).

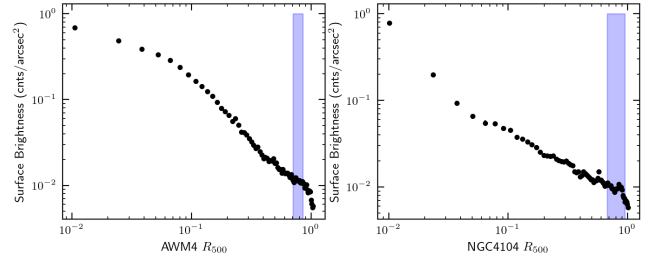


Figure 1. Surface brightness profiles of AWM4 (left) and NGC4104 (right). The blue highlighted region shows where the background region was defined.

On-chip backgrounds were determined outside of R_{500} for 23 of the systems. NGC4104 and AWM4 have R_{500} values of $14.8'$ and $14.1'$, respectively. That means the cluster takes up nearly the entire FOV of the XMM Newton MOS and PN chips, making it impossible to get an on-chip background outside of R_{500} . For these clusters, we took background regions that were as far away from the center of the cluster as possible. These backgrounds were selected based on the radial surface brightness profiles, shown in Figure 1, as the shaded regions where cluster brightness is negligible. If there was excess cluster signal in the chosen background, it would get modeled out at part of the background decreasing the fit Z_{ICM} . However, that does not seem to be the case as both clusters have fit Z_{ICM} higher than, or approximately the mean Z_{ICM} at their respective M_*/M_{gas} .

We first fit the background spectra using XSPEC (version 12.12.1c)³ to determine the background contribution. We modeled the background emission as two gaussian models to capture the XMM Newton instrumental lines, and three *apec* models for the Milky Way Local Hot Bubble and the warm- and hot-Milky Way halo components. For the former we assume solar abundance and an initial temperature of 0.1 keV, and for the latter we assume an abundance of $0.3Z_{\odot}$ and initial temperatures of 0.3 keV and 0.7 keV, respectively. We multiply the warm- and hot-Milky Way halo component by a *tbabs* model to account column absorption. The plasma temperatures are allowed to vary but consistently checked to ensure they are physical. A broken powerlaw with index 1.46 is also included for any residual soft proton background. We assume abundances from Asplund et al. (2009). These model components were frozen while fitting for cluster emission. This methodology ensures that our background is purely background as any overlap of the background re-

¹ <https://www.cosmos.esa.int/web/xmm-newton/sas>

² <http://xcx.harvard.edu/caldb/>

³ <https://heasarc.gsfc.nasa.gov/docs/xanadu/xspec/issues/archive/issues.12.>

gion with group or cluster emission would result in poor fit statistics.

We add an additional *apec* and *tbabs* for the cluster component. Constants are included to account for differences in solid angle so that spectra from neighboring annuli may be fit simultaneously, allowing for better consideration of the PSF. Finally, we include an additional *broken-powerlaw* and absorbed *apec* model for the quiescent particle background and to link the models for the respective crossarfs.

2.2. Chandra Data

We chose not to include Chandra observations in this study as Chandra’s smaller effective collecting area and lower spectral resolution make it less optimal for our analysis objectives. Due to the reduced collecting area, we are unable to obtain on-chip background measurements for all clusters in our sample. The lower spectral sensitivity further limits our ability to obtain reliable spectral fits in the outer annuli. We found that for 75% of the clusters only one or two annuli contributed to Z_{ICM} since not all three outer annuli could be extracted or fit. This restriction could bias Z_{ICM} toward higher values, given the typical radial decrease in Fe and our inability to probe larger radii.

We compared Z_{ICM} measurements with and without Chandra observations to ensure the validity of this decision. All data analysis and reduction was done using standard reduction practices, as outlined by the extended source analysis guide⁴. Including measurements from Chandra altered Z_{ICM} by 4% on average. This modest change stems from the larger uncertainties on metallicity values derived from Chandra, compared to those obtained with XMM Newton. The larger errors result in lower weights on the calculation of Z_{ICM} and our inability to include the outer annuli due to the chip size restrictions of Chandra or insufficient photon statistics. For these reasons, we have chosen not to incorporate archival Chandra data in our analysis.

2.3. Anomalous Systems

We identified an additional two clusters in Laganá et al. (2013) that met the criteria, however, in a further study, neither system is suitable for the study as we limit this study to virialized systems. Galaxy cluster A115 is a merging cluster with two asymmetric X-ray peaks and a radio feature (e.g., Barrena et al. 2007; Kim et al. 2019). We cannot assume azimuthal symmetry for the X-ray emission of this cluster because of the merg-

ing X-ray halos and therefore exclude this cluster for our survey.

The second group is NGC5098. This system did not initially present as unusual in its X-ray characteristics, however the determined $Z_{ICM} = 0.150 \pm 0.007$ is over 7σ away from NGC4325, the next-lowest Z_{ICM} , with Z_{ICM} of 0.205 ± 0.016 . We have chosen to exclude NGC5098 from the survey and any subsequent analysis due to its unusually low Z_{ICM} .

2.4. Survey Fit Results

The fit results are described in Tables 2 and 4 for the kT and Z_{ICM} fit values, respectively.

A couple of the observations lacked signal to obtain fit values in the outermost bin. Those bins are left blank in the tables. Other bins are defined by a single value without an error, due to nonphysical kT values being fit otherwise. For those fits, we froze the plasma temperature to a single value in order to obtain a reasonable fit, reduced $\chi^2 < 2$. The frozen plasma temperature was either determined by neighboring bins, or fit results from other observations of the same cluster in the same bin. We ensured that the frozen kT value did not significantly alter the resulting fit of the metallicity and therefore not arbitrarily determining Z_{ICM} .

In Figure 2 we show the fit metallicity radial trend of all the clusters within our sample (black line), $Z(R)$ (further discussed in Section 4.2). We determine the average $Z(R)$ as the weighted average (black data points and trend) and the median (blue data points and trend). The weighted average trend shows a decreasing $Z(R)$, consistent with Mernier et al. (2017) and simulations (Rasia et al. 2015; Nelson et al. 2024). However, the weighted average emphasizes clusters with smaller uncertainties, potentially biasing the measurement to brighter or more nearby clusters. The median trend is less susceptible to outliers and finds a flatter trend, and it therefore more representative of a typical system. Works such as Molendi et al. (2016), Lovisari & Reiprich (2019), and Ghizzardi et al. (2020) find a $Z(R)$ over various cluster types and outer radii. However, we note that our systems are not separated by type (i.e., cool core vs non cool core (Mernier et al. 2017), relaxed vs disturbed (Lovisari & Reiprich 2019)), and we do not isolate the Fe K α line as done in Ghizzardi et al. (2020), instead relying on broad-band spectral fitting.

3. DETERMINING METALLICITY CONTRIBUTIONS TO Z_{ICM}

The values of Z_{ICM} are determined as the weighted average of the fit metallicity values in the outer three annuli. The center two annuli are excluded as there is a

⁴ <https://cxc.cfa.harvard.edu/ciao/guides/esa.html>

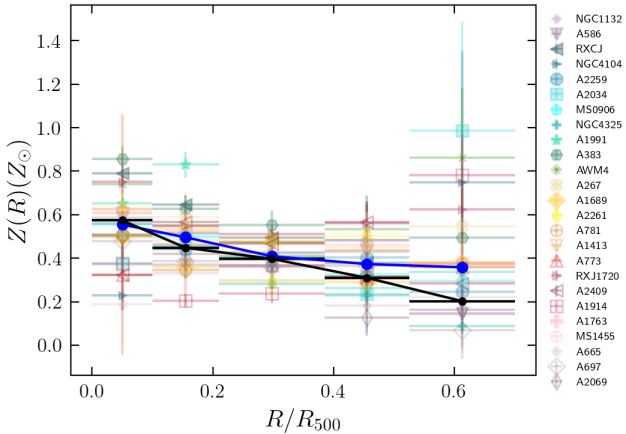


Figure 2. Radial trend of the fit metallicity for all clusters. We show the weighted average (black points) and median (blue points) within each bin. The median trend flattens out to a mean metallicity of $0.37Z_{\odot}$ in the outer radial bins. The weighted average trend shows a negative trend of Z_{ICM} with radius best described by a line with slope -0.70 ± 0.04 and intercept 0.57 ± 0.01 .

known central peak in abundance due to the presence of the BCG (De Grandi et al. 2004; Mernier et al. 2017). We show the relationship of Z_{ICM} and M_*/M_{gas} in Figure 3. The data points show some scatter but follow a seemingly straight line. We use the methodology described in Section 2.4 of Sharma (2017) to fit the data with a straight line. The values of M_*/M_{gas} are fit in log-space due to their spread over an order of magnitude. In a future work we investigate potential physical motivations for $\log M_*/M_{gas}$ among cluster parameters (Gherri et al., in prep). This methodology also allows for consideration of both the x and y errors. The result of this fit is presented in Equation 1, and shown as the solid red line in the top left panel of Figure 3.

$$Z_{ICM} = -0.08_{-0.07}^{+0.07} \log \left(\frac{M_*}{M_{gas}} \right) + 0.30_{-0.06}^{+0.06} \quad (1)$$

The original fit results in a reduced $\chi^2 = 5.14$. We introduce a term for intrinsic scatter, σ_p in the fit in order to obtain a reasonable fit. The factor σ_p is determined to be $0.09_{-0.01}^{+0.02}$, resulting in a reduced $\chi^2 = 0.91$.

We also exclude the three most anomalous systems, NGC1132, NGC5098, and NGC4325 and refit for Z_{ICM} finding,

$$Z_{ICM} = 0.06_{-0.05}^{+0.06} \log \left(\frac{M_*}{M_{gas}} \right) + 0.46_{-0.05}^{+0.05}. \quad (2)$$

The fit returns a reduced $\chi^2 = 2.58$ without an intrinsic scatter. When including intrinsic scatter in the fit we obtain $\sigma_p = 0.05_{-0.01}^{+0.02}$ resulting in a reduced $\chi^2 = 0.93$.

This fit is presented as the bottom right panel in Figure 3. The other two panels in Figure 3 show the intermediate fits, excluding a single cluster at a time. Further discussion on the nature of these systems is presented in Section 4.2.

3.1. Determining Z_*

We first must determine the contribution of the visible stellar populations to Z_{ICM} , Z_* , in order to isolate the contribution of the EEP to Z_{ICM} , Z_{EEP} , as $Z_{EEP} = Z_{ICM} - Z_*$. The first assumptions we make to determine Z_* are that we are working with a closed box model and constant star formation. For the most massive systems the deep gravitational potential wells are sufficiently strong that most of the baryons are retained (e.g., Kravtsov & Borgani 2012a, and references therein). However, simulations and observations indicate departures from this assumption in lower-mass systems, which are more susceptible to baryon loss (Bregman et al. 2010). The closed-box assumption may be appropriate for the high-mass systems, but it should be interpreted with caution, as its applicability decreases for lower-mass systems.

We begin by defining metallicity as the mass of metals, M_z , over the gas mass, M_{gas} , $Z = \frac{M_z}{M_{gas}}$. Therefore, the change in metallicity over some time step is given by Equation 3.

$$dZ = d \left(\frac{M_z}{M_{gas}} \right) \quad (3)$$

Differentiating this, we get

$$dZ = \frac{1}{M_{gas}} (dM_z - \frac{M_z}{M_{gas}} dM_{gas}). \quad (4)$$

We must now introduce more assumptions about the metal production and incorporation. The metal mass initially locked up in stars, M_* , decreases at the same rate M_{gas} increases during a single time step. That is, $-dM_* = dM_{gas}$. For this to be correct, we make the assumption of instantaneous mixing of metals with the ICM. Finally, the mass of metals, dM_z , increases as the metals produced by stars, dM_* , multiplied by some yield, y . We substitute $dM_z = ydM_* - ZdM_*$ into Equation 4, and use $dM_* = -dM_{gas}$ in order to define Z solely in terms of M_{gas} .

$$dZ = \frac{1}{M_{gas}} (-ydM_{gas} + ZdM_{gas} - ZdM_{gas}). \quad (5)$$

This gives us the final relationship of

$$dZ = -y \frac{dM_{gas}}{M_{gas}} \quad (6)$$

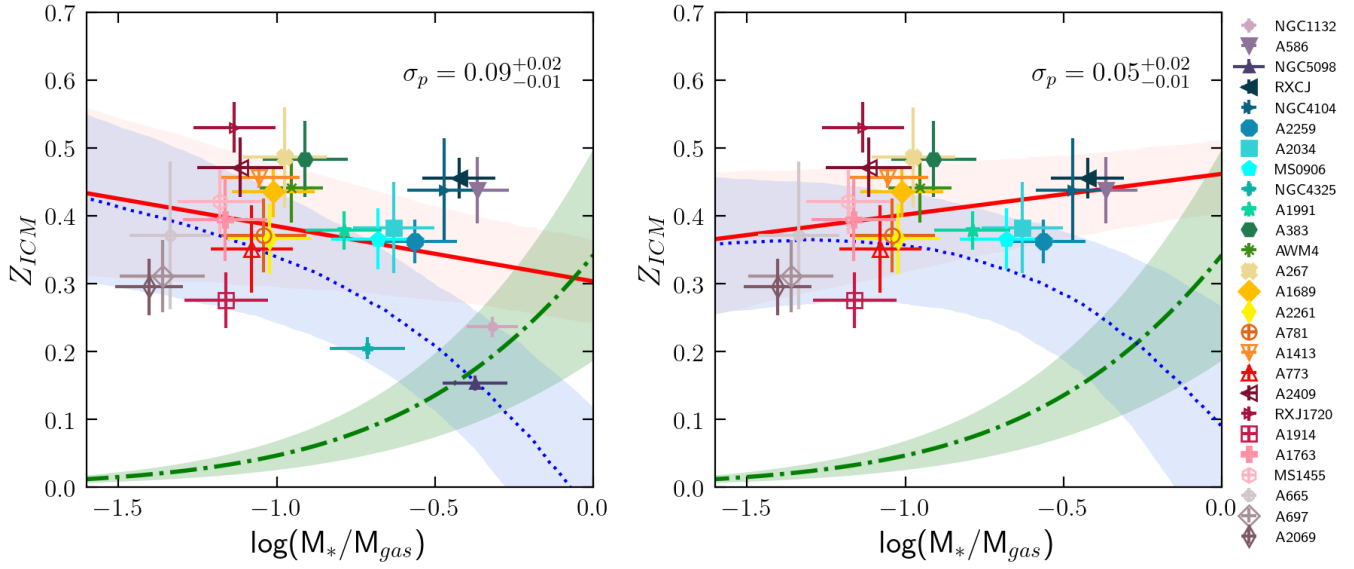


Figure 3. Left: We present the fit relationship of Z_{ICM} vs M_*/M_{gas} for all 26 groups and clusters. We find $Z_{ICM} = -0.08^{+0.07}_{-0.07} \log\left(\frac{M_*}{M_{gas}}\right) + 0.30^{+0.06}_{-0.06}$ with an intrinsic scatter of $\sigma_p = 0.09^{+0.02}_{-0.01}$ (red solid line). This fit was done using techniques described in [Sharma \(2017\)](#). The derived trend of Z_* (green dash-dot, Equation 15) is subtracted from Z_{ICM} to find $Z_{EEP} = \log_{10} \left[\left(\frac{M_*}{M_{gas}} \right)^{-0.08^{+0.07}_{-0.07}} \left(1 + \frac{M_*}{M_{gas}} \right)^{1.14 \pm 0.52} \right] + 0.30^{+0.06}_{-0.06}$ (blue dotted line). All shaded regions show the 1σ confidence intervals.

Right: Total fit excluding NGC5098, NGC4325, and NGC1132 to determine a fit of Z_{ICM} versus M_*/M_{gas} as $Z_{ICM} = 0.06^{+0.06}_{-0.05} \log\left(\frac{M_*}{M_{gas}}\right) + 0.46^{+0.05}_{-0.05}$ and $\sigma_p = 0.05^{+0.02}_{-0.01}$, shown as the red solid. We subtract off the derived Z_* (green dash-dot line) to derive $Z_{EEP} = \log_{10} \left[\left(\frac{M_*}{M_{gas}} \right)^{0.06^{+0.06}_{-0.05}} \left(1 + \frac{M_*}{M_{gas}} \right)^{1.14 \pm 0.52} \right] + 0.46^{+0.05}_{-0.05}$ (blue dotted line). The derived reduced χ^2 is ~ 0.90 for all four fits, however the required σ_p (printed in the top right corner of all plots) to keep the χ^2 at an acceptable value decreases as the number of potential outliers excluded increases.

We now integrate Equation 6 from 0 to t to get the total metallicity,

$$Z(t) = -y \log\left(\frac{M_{gas}(t)}{M_{gas}(0)}\right). \quad (7)$$

We next rewrite Equation 7 in terms of M_*/M_{gas} to allow comparison with our fit trend of Z_{ICM} vs M_*/M_{gas} . The term M_{gas} can be expressed as $M_{gas}(t) = M_{tot} - M_*(t)$. At $t = 0$ we assume the system to be composed entirely of gas meaning $M_{gas}(0) = M_{tot}$. Equation 7 then becomes,

$$Z(t) = y \log\left(1 + \frac{M_*}{M_{gas}}\right). \quad (8)$$

The remaining factor to define is the yield of Type Ia supernovae (SN Ia) and core collapse supernovae (SNCC), y . This was thoroughly discussed and derived in Loewenstein (2013) who considered factors such as supernova rate, mass return fraction, and metals locked in stars. From Equations 13 and 19, we adopt an equation for yield as

$$y_i = \eta^{SN}(1 - r_*)^{-1}(1 + R_{SN})^{-1}(y_i^{cc} + R_{SN}y_i^{Ia})f_{i,\odot} \quad (9)$$

where η^{SN} is the specific number of supernova explosions per star formed, r_* is the fraction of mass previously formed into stars and recycled back into gas, $R_{SN} = \frac{\eta^{Ia}}{\eta^{cc}}$, y_i^{cc} and y_i^{Ia} are the yields of the i th element per SNCC and SN Ia respectively, and $f_{i,\odot}$ is the solar mass fraction of the i th element.

We adopt $\eta^{Ia} = 3.1_{-1.0}^{+1.1} \times 10^{-3}$ from DTD fits in Freundlich & Maoz (2021). The value for η^{cc} is a little more complicated as it is not explicitly measured. Few sources state calculated values of η^{cc} such as 0.0068 from Madau & Dickinson (2014), 0.007 from Dahlen et al. (2012), and 0.008 from Loewenstein (2013). We assume a value of $\eta^{cc} = 0.0075 \pm 0.002$ to represent the average and encapsulate the range of η^{cc} presented in the literature. The error was chosen as it is approximately the same percent error as that on η^{Ia} , and encapsulates all possible η^{cc} . These values, however, do not account for the metals locked up in stars. We adopt Equations 20 and 21 from Loewenstein (2013) as correction factors for metals locked up in stars for SN Ia and SNCC, respectively.

Ma et al. (2025) performed a recent survey using wide-field surveys from 2016-2023 to determine the fractional rates of SN Ia and SNCC. They found $\frac{N_{*}^{Ia}}{N_{*}^{SN}} = 33.4_{-11.5}^{+3.7}\%$ and $\frac{N_{*}^{cc}}{N_{*}^{SN}} = 69.6_{-20.1}^{+10.2}\%$. The later value was determined by adding together the determined fractions for SNe Ibc and SNe II from Ma et al. (2025). We multiply these values by the previously determined $\frac{N_{*}^{SN}}{M_*} =$

$\eta^{Ia} + \eta^{cc} = 0.011 \pm 0.002$ to find $\eta_*^{Ia} = (2.1 \pm 0.7) \times 10^{-3}$, and $\eta_*^{cc} = (4.8 \pm 1.5) \times 10^{-3}$. Finally, we subtract the metals locked up in stars from the total available enrichment as given in Equations 22 and 23 in Loewenstein (2013) to find $\eta_{ICM}^{Ia} = (1.0 \pm 1.1) \times 10^{-3}$ and $\eta_{ICM}^{cc} = (2.7 \pm 1.6) \times 10^{-3}$.

The final correction factor is the mass return fraction, r_* . We use Equation 6 and the cut-off points determined in Madau & Dickinson (2014) to determine $r_* = 0.35$ for a diet-Salpeter IMF.

3.1.1. Metals Locked in Remnants

One additional correction to consider is the metals locked in remnants. Throughout this derivation we have assumed constant star formation. This means that there will be an increasing number of remnants that have locked up enriched gas from previous stellar populations. The remnants we consider are neutron stars (NS) and black holes (BH) for SNCC, f^{cc} , and white dwarfs (WD) that are not in binary systems for SN Ia, f^{Ia} .

Kobayashi et al. (2006) provides metal yields that incorporate remnant metal lockup. However, their approach simplifies aspects of remnant formation and metal retention, such as fixed remnant masses as a function of progenitor mass, survival fraction of WD, SN Ia pathways, binary fraction uncertainties, and the possibility of black holes being ‘‘born in the dark’’. More generally, studies of chemical evolution (e.g., Werner et al. 2008; de Plaa et al. 2017; Simionescu et al. 2019) find discrepancies when using standard yield sets, including Kobayashi et al. (2006). This implies that a more nuanced treatment of the counting the metal budget is required. Additional corrections must be applied to adequately capture the range of plausible scenarios for metal lock-up in remnants. We continue with a study of metal lockup in remnants using a Bayesian approach.

The remnant lockup correction factors can be defined as

$$f^{Ia} = \frac{N_{WD}^{Ia}}{N^{Ia}} \quad (10)$$

and

$$f^{cc} = \frac{N_{NS}^{cc} + N_{BH}^{cc}}{N^{cc}}, \quad (11)$$

where

$$N_{rem}^i = \int_{m_{lo}}^{m_{hi}} \phi(m) \frac{M_{rem}(m)}{m} dm, \quad (12)$$

and

$$N^i = \int_{m_{lo}}^{m_{hi}} \phi(m) dm. \quad (13)$$

We define m_{hi} and m_{lo} as the high and low mass cutoff for progenitor stars, $M_{rem}(m)$ as the relationship between the progenitor and the remnant mass, and the IMF as $\phi(m)$.

The correction factor is applied to η_{ICM} as,

$$\eta^{SN} = \eta_{ICM}^{cc}(1 - f^{cc}) + \eta_{ICM}^{Ia}(1 - f^{Ia}) \quad (14)$$

There is a significant amount of uncertainty surrounding the formation pathways of SN Ia, and the remnants of BHs. To account for this, we adopt a Bayesian framework using estimates and formation theories from the literature as priors for calculations of N_{BH}^{cc} and N_{WD}^{Ia} .

We consider WDs that are completely destroyed in SN Ia and those that are not in binary systems for the priors on N_{WD}^{Ia} . There is no lockup correction when the WD is completely destroyed in a SN Ia, providing a lower prior constraint of $N_{WD}^{Ia} = 0$. The upper constraint is calculated by assuming $M_{rem}(m)$ from Cummings et al. (2018), a progenitor mass range of $3-8M_{\odot}$, and a binary fraction of 46% (Raghavan et al. 2010). This results in an upper limit of $N_{WD}^{Ia} = 2.69 \times 10^{-3}$. We note that both models for $M_{rem}(m)$ provided by Cummings et al. (2018) (Equations 3 and 8) result in values of N_{WD}^{Ia} within 4%.

We must consider formation theories to determine the priors for BHs. The first of the two competing BH formation theories is that they leave behind a remnant (Blundell et al. 2008; Balakrishnan et al. 2023). The second is they are ‘‘born in the dark’’ and are not associated with a remnant. A BH ‘‘born in the dark’’ would result in no emission of stellar material into the ICM, resulting in an upper limit of $f^{cc} = 1$, and therefore $N_{BH}^{cc} = 8.748 \times 10^{-3}$. We assume a progenitor mass range for BHs of $25 - 150M_{\odot}$ when considering that a BH leaves behind a remnant. The lower limit of $25M_{\odot}$ follows from adopting a progenitor mass range for NS of $8 - 25M_{\odot}$ Fryer (1999); Belczynski & Taam (2008). The upper limit is that of the diet-Salpeter IMF. We adopt $M_{rem}(m) = 10M_{\odot}$ (Heger & Woosley 2002), resulting in a lower limit of $N_{BH}^{cc} = 2.17 \times 10^{-3}$.

We do not pose any priors on N_{NS}^{cc} and simply adopt a progenitor mass range of $8 - 25M_{\odot}$, and $M_{rem}(m) = 1.4M_{\odot}$, calculating $N_{NS}^{cc} = 4.19 \times 10^{-3}$.

Finally, we impose a physical lower limit of 0 to the determination of η^{SN} . These priors and constraints result in $\eta^{SN} = 3.5_{-2.1}^{+4.8} \times 10^{-3}$. The posterior distribution is shown in Figure 4.

The final trend for Z_* is given as Equation 15.

$$Z_* = (1.14 \pm 0.52) \log\left(1 + \frac{M_*}{M_{gas}}\right) \quad (15)$$

3.2. Z_{EEP}

The trend of Z_{EEP} is calculated by subtracting the expected contribution from the visible stellar populations, Z_* , from the fit trend of Z_{ICM} . Including the

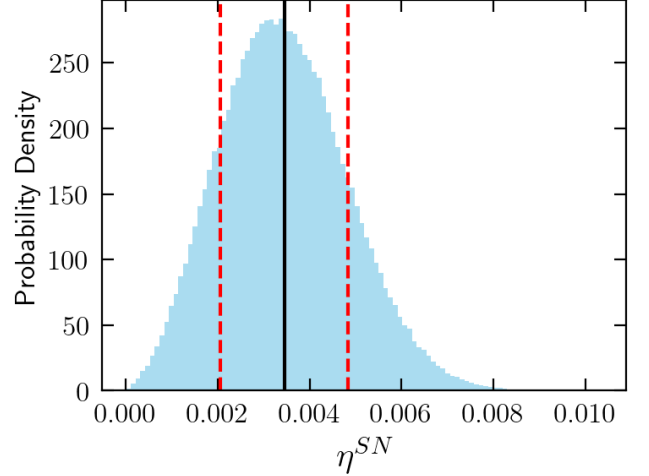


Figure 4. Posterior distribution of η^{SN} . The black vertical line shows the mean value of 0.0035, with 1σ shown by the dashed red lines.

entire data set, we find

$$Z_{EEP} = \log_{10} \left[\left(\frac{M_*}{M_{gas}} \right)^{-0.08_{-0.07}^{+0.07}} \left(1 + \frac{M_*}{M_{gas}} \right)^{1.14 \pm 0.52} \right] + 0.30_{-0.06}^{+0.06} \quad (16)$$

Excluding the outliers NGC1132 and NGC4325, Z_{EEP} , we determine

$$Z_{EEP} = \log_{10} \left[\left(\frac{M_*}{M_{gas}} \right)^{0.06_{-0.05}^{+0.06}} \left(1 + \frac{M_*}{M_{gas}} \right)^{1.14 \pm 0.52} \right] + 0.46_{-0.05}^{+0.05} \quad (17)$$

The top left and bottom right panels of Figure 3 show all three derived components.

4. DISCUSSION

Our uniform analysis of 26 galaxy groups and clusters points to the necessity of including an EEP when considering the contributions to Z_{ICM} . Conventional closed-box chemical evolution models assume all metals are produced and retained by the visible stellar populations with more modern-day IMFs. These classical models fail to reproduce the observed trends of Z_{ICM} vs M_*/M_{gas} , and systematically under predict Z_{ICM} , especially in systems with low M_*/M_{gas} . This discrepancy strongly suggests that an additional population of stars, now absent or undetectable, must have contributed significantly to the ICM metal budget.

The observed trend of M_*/M_{gas} serves as a powerful constraint on the nature and origin of the EEP. It

implies that these stars must have formed early, likely pre-reionization (B25), and efficiently enriched the gas. As such, the trend can be used as a diagnostic to infer key properties of the EEP, such as its IMF, time of formation, and SN Ia rate as a function of redshift as done in B25.

We continue to explore the implications of several key assumptions in this model framework and discuss the influence of outlier systems on the inferred enrichment trends.

4.1. Z_* Assumptions

The trend of Z_{EEP} is inherently dependent on the derived Z_* . This dependence makes our understanding of the present-day stellar populations within clusters and groups crucial. Any uncertainty or systematic bias in Z_* from observational limits, stellar population synthesis models, or assumptions of chemical yields and evolution directly propagates to Z_{EEP} .

Few works have performed a full analytic derivation of Z_* (e.g., Loewenstein 2013; Blackwell & Bregman 2025). We adopt the derivation for y from Loewenstein (2013), but adopt more modern values and add additional consideration for metals locked in remnants. Therefore, our derived y is similar to, but lower than $y = 1.55$ as estimated in Loewenstein (2013). B25 derived a line fit for Z_* assuming that the highest stellar fraction system, NGC1132, would have $Z_{ICM} = Z_*$ finding $Z_* = 0.63 \pm 0.12(M_*/M_{gas})$.

One of the primary assumptions in the calculation of y (the slope of Z_*) is the formation pathway of BHs. For the upper limit, we use the assumption that BHs are “born in the dark”. That is, all of the progenitor stellar material goes into the formation of the black hole and no remnant is left behind. For the lower limit, we assume that a remnant is left behind when a BH is formed and that $M_{rem}^{BH} = 10M_\odot$ Heger & Woosley (2002). We tested the impact of this assumption on the derivation of y by stepping through assumed values of M_{rem}^{BH} from 5-150 M_\odot in steps of 5 M_\odot from 5-45 M_\odot and steps of 25 M_\odot from 50-150 M_\odot . Figure 5 shows the resulting y values. We find that the assumption of M_{rem}^{BH} does not change our trend of Z_* , as y is determined within 1 σ for the full range of M_{rem}^{BH} .

We consider the result of this in relation of the “born in the dark” theory. Assuming $M_{rem}^{BH} = 150M_\odot$ implies all progenitor stellar mass for the highest mass stars permitted by our assumed IMF collapses into the BH. That is, there is no contribution of BH progenitors to Z_{ICM} . This results in $y = 0.724 \pm 0.519$, within 1 σ of $y = 1.19 \pm 0.53$ derived with $M_{rem}^{BH} = 5M_\odot$. This lack of dependence of the yield on M_{rem}^{BH} may indicate

that BHs and their associated nebula do not contribute significantly to Z_{ICM} . We must also consider that this trend, or lack thereof, makes sense in the context of Fe as it dominates our measurements of Z_{ICM} . The byproducts of SNCC are mainly elements α , which makes Fe a poor tracer of the dependence of y on M_\odot . Future work using measurements of α elements to trace the contribution of SNCC would be necessary to make any general conclusions using this framework.

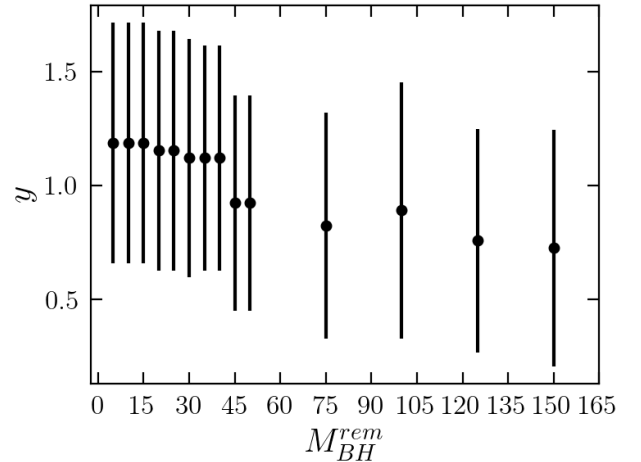


Figure 5. Relationship between the derived y , the yield from SNe when accounting for metals locked up in stars and remnants, as a function of assumed mean BH remnant mass, M_{BH}^{rem} . All resulting y values are within 1 σ indicating only a weak dependence on M_{BH}^{rem} .

We also use the derived trend of Z_* , and assumptions made within, to determine the partitioning of metals in the gas, stellar, and remnant phases as a function of M_*/M_{gas} , Figure 6. We find that the majority of metals reside in the hot gas phase for systems with low stellar mass fractions. As M_*/M_{gas} increases, a progressively larger fraction is locked in stars. However, the fraction of metals locked in remnants remains nearly constant across the sample.

These findings are supported by observations and theoretical models in that a majority of metals are retained in the ICM. Findings from Ghizzardi et al. (2020) support our conclusions as they find that the iron share ($M_{Fe,500}/M_{Fe,500}^*$) is approximately a factor of 10. However, they note that large systematic uncertainties prevents them from drawing firm conclusions. Sivanandam et al. (2009) shows that the BCG and ICL produce and contribute 22 – 31% of metals in the ICM, a fraction broadly comparable to the metals fraction locked in stars. The relatively minor metal fraction in remnants agrees with expectations of stellar evolution and feed-

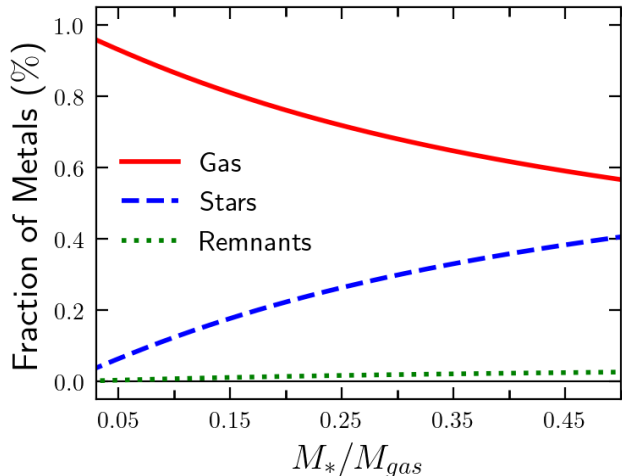


Figure 6. Fraction of metals the in gas phase (red line), locked in stars (blue dashed line), and remnants (green dotted line) as a function of M_*/M_{gas} .

back models (e.g., Nomoto et al. 2013, and references therein).

4.2. NGC1132, NGC4325, and NGC5098

Three systems in our sample, NGC1132, NGC5098, and NGC4325, stand out as potential outliers. All systems have a high M_*/M_{gas} and low Z_{ICM} , as summarized and presented in Table 1. Determining whether these systems are genuine outliers requires careful consideration of the adopted fit and σ_p and the physical characteristics of each system.

We first consider the full set of 26 groups and clusters. Relative to the best-fit model, NGC1132, NGC5098, and NGC4325 lie -0.22σ , -1σ and -0.72σ away, respectively. However, an intrinsic scatter of $0.09^{+0.02}_{-0.01}$ required to obtain an acceptable fit statistic. These systems also have considerable influence on the overall fit, altering the slope, intercept, and required intrinsic scatter by $\sim 2\sigma$ when they are included vs excluded from the sample.

We consider a second case to derive a value of σ_p that may be more representative of the survey and determine if the anomalous groups are statistical outliers. For this we look at 16 systems with M_*/M_{gas} between 0.040–0.12 clustered with a mean $Z_{ICM} = 0.40Z_{\odot}$. We assume a fit to this clump with $m = 0$ and $b = 0.40$ and find $\sigma_p = 0.04$ is required to achieve a fit within the 95% confidence level. We find that NGC1132, NGC5098, and NGC4325 are -3.8σ , -5.9σ , and -4.5σ , respectively. The three anomalous systems are certainly outliers in this fit scenario. We also compare the three systems to the fit of all 26 systems ($m = -0.08 \pm 0.07$, $b = 0.30 \pm 0.06$), adopting the determined intrinsic scatter of 0.04. These systems fall within -0.46σ , -2.21σ , and -1.76σ

for NGC1132, NGC5098, and NGC4325, respectively. In this case, only NGC5098 lies $> 2\sigma$ away from the line of best fit and may be considered an outlier.

Based solely on statistics, we only consider NGC5098 to be an outlier as it consistently lies $> 2\sigma$ away from the line of best fit. We determine NGC1132 and NGC4325 to be anomalous, but not full outliers, since they are within $\sim 1.5\sigma$ of the derived trends. While deviations of this magnitude indicate that these systems lie toward the extremes of the distribution, a 1.5σ offset corresponds to a confidence level of roughly 86.6% indicates that these systems lie toward the extreme and does not strongly reject the null hypothesis that they belong to the same initial population. Statistical significance alone is insufficient for definitive outlier classification, making it essential to complement this analysis with a study of the physical properties and environmental context of these systems. This approach ensures that natural variations and measurement uncertainties are properly accounted for before classifying these systems as true outliers.

A key distinguishing feature of each group is their radial metallicity trend, shown in the left panel of Figure 7. NGC1132, NGC5098, and NGC4325 all exhibit steadily declining $Z_{ICM}(R)$ profiles with particularly small measurement uncertainties. This is in contradiction to the radial trends of all 26 systems ($n=26$) and the sample excluding the three anomalous systems ($n=23$) which flatten at high radii to $0.37Z_{\odot}$. This suggests that the trend of the three anomalous systems are not representative of the general group and cluster sample.

Cosmological simulations predict varied metallicity gradients depending on the epoch and efficiency of enrichment. Simulations by Tornatore et al. (2007) and Rasia et al. (2015) find decreasing radial metallicity trends, with steeper gradients in cool-core (CC) clusters. In contrast, simulations by Biffi et al. (2017) find a flat radial metallicity trend with a mean $Z_{ICM} = 0.28 \pm 0.03Z_{Fe,\odot}$. This work uses the same metal enrichment scheme as Tornatore et al. (2007), but with the key difference of early ($z > 2 - 3$) AGN feedback, allowing metal mixing with ICM. These studies demonstrate that the slope of $Z_{ICM}(R)$ depends on the timing of star formation and the strength and epoch of AGN feedback. Systems that form earlier with AGN feedback display a flatter Z_{ICM} distribution, while later forming groups with less AGN activity tend to centrally peaked and steeper Z_{ICM} profiles. The declining trends in our three anomalous systems qualitatively resemble predictions for groups that experienced relatively late enrichment and mixing, after reionization and contribution from the EEP.

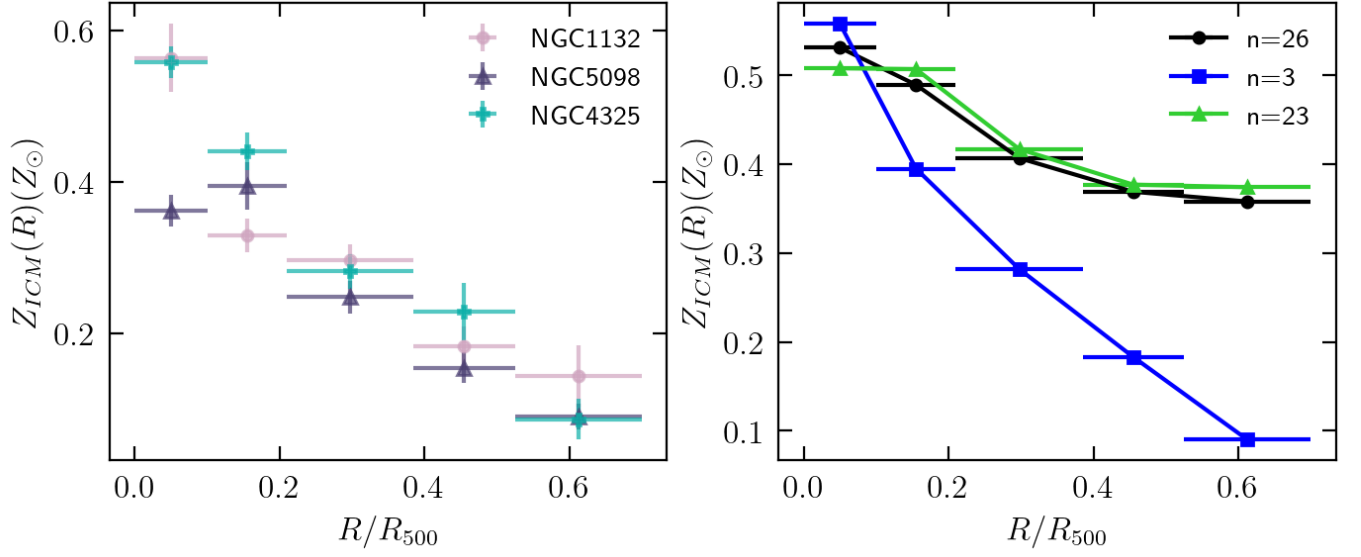


Figure 7. Left: Radial metallicity trends of NGC1132 (pink circles), NGC5098 (purple triangles), and NGC4325 (blue plus). Each trend is a tightly constrained and steadily decreasing with a powerlaw slope of approximately $R^{-0.5}$. **Right:** Comparison of median radial metallicity trends for samples including all 26 systems ($n=26$, black), just NGC1132, NGC5098, and NGC4325 ($n=3$, blue), and the full sample excluding NGC1132, NGC5098, and NGC4325 ($n=23$, green). Excluding the three anomalous systems from the full sample, $n=23$, results in a much flatter Z_{ICM} distribution with an average $Z_{ICM} = 0.37Z_{\odot}$ in the outer radii. This trend is in good agreement with that of the full data set, $n=26$. This highlights how unique NGC1132, NGC5098, and NGC4325 are from the rest of the sample.

The individual properties of these systems also support the interpretation that they may have followed atypical assembly histories and separate them from the rest of the survey. NGC1132 is classified as a fossil group, hosts a cool core, and has a relatively low halo mass $M_{gas,500} = (1.24 \pm 0.03) \times 10^{12} M_{\odot}$ (Mulchaey & Zabludoff (1999); Russell et al. (2007); Laganá et al. (2013); Kim et al. (2018)), consistent with efficient cooling after recent disturbance. NGC5098 shows disturbed kinematics, including gas sloshing, X-ray cavities correlated with radio emission, extended intragroup light, and asymmetric temperature and metallicity distributions (Randall et al. 2009; Lima Neto et al. 2025), all indicative of recent formation and ongoing mixing. NGC4325, although also a cool core group, contains a Fe-rich bar-shaped structure in its center (Laganá et al. 2015), suggesting incomplete mixing and late-time enrichment. Laganá et al. (2015) also determined the kT and Fe radial trends which are in good agreement with ours when considering that we have additional radii $> 150''$ that extend to larger radii. Together, these kinematic anomalies set these groups apart from the rest of our survey and are consistent with systems with more recent formation histories.

Altogether this suggests that NGC1132, NGC5098, and NGC4325 are outliers. We posit that these groups formed after the peak enrichment of the EEP and post-reionization. In this scenario, the current stellar populations of these groups would enrich the ICM, meaning their $Z_{ICM} \propto Z_*$, as seen in Figure 3. Present day stellar enrichment would also result in declining $Z_{ICM}(R)$ and low Z_{ICM} compared to systems that may have had a period of early AGN feedback. Positioning these systems in a broader theoretical context highlights the necessity of cosmological simulations for linking metallicity gradients to assembly histories (e.g., Tornatore et al. 2007; Rasia et al. 2015; Biffi et al. 2017, 2018). This has motivated further investigations into whether other distinct populations exist in the Z_{ICM} vs M_*/M_{gas} phase-space, and is the focus of a future work (Gherri et al., in prep).

4.3. Revisiting the Closed-box Assumption

A closed-box model is often assumed for studies of chemical evolution of galaxies and clusters (Pipino et al. 2002; Loewenstein 2013; Kudritzki et al. 2015; Wu et al. 2015, e.g.,). In this model, all of the gas and metals are retained in the gravitational potential well. This is a reasonable assumption for galaxy clusters as they are able to retain both primordial gas and processed metals (Kravtsov & Borgani 2012b). Thus we expect the observed baryon fraction to closely trace the cosmic

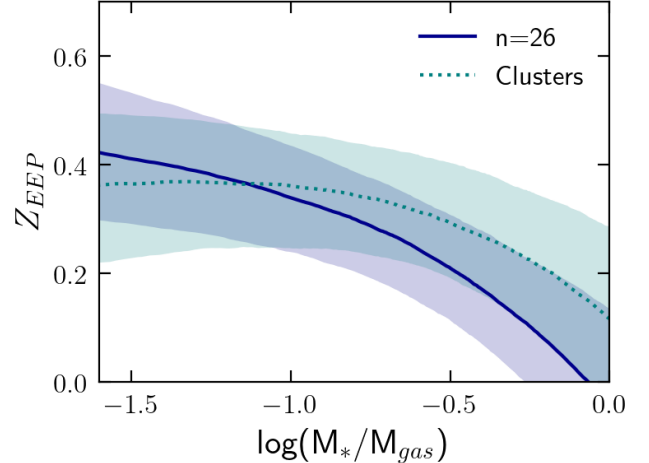


Figure 8. We compare the derived trends of Z_{EEP} for the full sample ($n=26$, blue solid line) and just the galaxy clusters (dotted teal line). The shaded regions represent the 1σ region. The mean trend of Z_{EEP} for both samples is within 1σ of the other.

mean value and Z_{ICM} to trace the integrated stellar yield (Ettori et al. 2009; Pratt et al. 2019).

Galaxy groups have much shallower gravitational potential wells and processes such as AGN-driven outflows may result in the loss of baryons such as hot gas and metals (McCarthy et al. 2010; Young et al. 2011; Lovisari et al. 2015; Paul et al. 2017; Eckert et al. 2021; Roper et al. 2025). We see this in our sample resulting in lower baryon fractions for the groups, $f_{b,g} = 0.127 \pm 0.011$ than clusters, $f_{b,c} = 0.156 \pm 0.003$. This loss of mass in groups may bias yield estimates as groups lose a greater fraction of metals per stellar mass formed, artificially steepening the relationship of Z_{ICM} vs $\log(M_*/M_{gas})$.

We tested these systematic differences by removing the nine galaxy groups from our sample and re-deriving Z_{EEP} , Equation 18.

$$Z_{EEP} = \log_{10} \left[\left(\frac{M_*}{M_{gas}} \right)^{0.05 \pm 0.07} \left(1 + \frac{M_*}{M_{gas}} \right)^{1.14 \pm 0.52} \right] + 0.45^{+0.08}_{-0.07} \quad (18)$$

The intrinsic scatter determined for this fit is $\sigma_p = 0.06^{+0.02}_{-0.01}$. These results remain consistent within 1σ when including or excluding galaxy groups (Figure 8).

The closed-box limitations for galaxy groups and variations in f_b must be acknowledged and carefully considered. However, the derived yields and primary conclusions for our cluster sample are not significantly affected by the properties of galaxy groups within our mass and redshift range.

4.4. IMFs

We next consider the implications of the assumed diet-Salpeter IMF. The diet-Salpeter IMF is a modified version of the traditional Salpeter IMF. This IMF introduces a break in the power-law slope at $1M_{\odot}$, with a flattening to $\alpha = -0.35$ in $\log(m)$ for stellar masses below this threshold. It also imposes a lower mass cutoff at $0.5M_{\odot}$. Above $1M_{\odot}$, the diet-Salpeter IMF is identical to the standard Salpeter IMF. The IMF primarily influences the determination of the stellar mass return fraction, r^* , and the core-collapse remnant fraction, f^{cc} . Because the high-mass end of the IMF remains unchanged, adopting the original Salpeter IMF does not alter our results. Additionally, deviations from other commonly used IMFs, such as Kroupa or Chabrier, are minor in this context as all derived quantities are well within 1σ (Kroupa 2001; Chabrier 2003).

5. SUMMARY

The presence of an EEP has broad implications for the history of star formation in the early Universe and the interpretation of chemical evolution in large-scale structures. The EEP may reflect a period of intense star formation of late Pop III and early Pop II stars potentially linked to early feedback processes that shaped the abundance of the ICM (Elbaz et al. 1995; Loewenstein 2013; Renzini & Andreon 2014; Blackwell & Bregman 2025).

There are limited constraints on the EEP, such as those in Loewenstein (2013) and B25. This is due to the reliance on uniform Z_{ICM} measurements and robust estimates of the metals contributed from the present day stellar populations Z_* . The goal of this survey was to perform a uniform analysis of 26 galaxy groups and clusters, with consistent measurements of $M_{*,500}$ and $M_{gas,500}$ to minimize uncertainties on Z_{ICM} , and therefore the metal contribution from the EEP Z_{EEP} . Here we summarize our key findings from this survey work:

1. We used an MCMC and fitting statistics defined in Sharma (2017) to fit the full sample of clusters to find Equation 1 with an intrinsic scatter of $\sigma_p = 0.09_{-0.01}^{+0.02}$ with a reduced $\chi^2 = 0.91$. Excluding likely outliers NGC1132, NGC5098, and NGC4325 we fit Equation 2 with an intrinsic scatter of $\sigma_p = 0.05_{-0.01}^{+0.05}$ with a reduced $\chi^2 = 0.93$.

2. We present a detailed look at the derivation of Z_* , demonstrating that the visible stellar populations alone systematically underpredicts the observed Z_{ICM} , particularly in systems with low M_*/M_{gas} . For this derivation, we begin with the assumption of a closed-box system, continuous star formation, and instantaneous mixing. We used the yield determination from Loewenstein (2013), and added an additional consideration of the metals locked in remnants to derive Z_* as presented in Equation 15.
3. We derive the inferred Z_{EEP} as the difference between $Z_{ICM} - Z_*$, presented in Equations 16 and 17. The best-fit relations in Equations 1 and 2 reveal a nearly flat or slightly increasing trend, reinforcing the need for an EEP.
4. We identified three outlier systems NGC1132, NGC5098, and NGC4325. They each exhibit low Z_{ICM} and pronounced negative radial Z_{ICM} trends, despite their high relatively M_*/M_{gas} . Their inclusion in global metallicity fits significantly affects the inferred slope and intrinsic scatter ($\sim 2\sigma$), highlighting their influence and uniqueness. We posit that these systems formed post-reionization after the rest of the systems within the sample and peak of the EEP. Such characteristics are consistent with cosmological simulations that show later forming groups tend to have steeper metallicity gradients and a lower Z_{ICM} (Tornatore et al. 2007; Rasia et al. 2015; Biffi et al. 2017).

This study confirms and quantifies the necessity of a population such as the EEP to explain Z_{ICM} . We provide a robust and testable framework for future theoretical and observational work on the origin and physical properties of the EEP.

6. ACKNOWLEDGMENTS

We greatly thank Cameron Pratt, Zhijie Qu, Rui Hang, and Jiangtao Li for thoughtful discussions, guidance, and feedback on this work. The authors would like to acknowledge the support from NASA ADAP Award 80NSSC22K0481 for this program.

REFERENCES

- Asplund, M., Grevesse, N., Sauval, A. J., & Scott, P. 2009, *ARA&A*, 47, 481, doi: 10.1146/annurev.astro.46.060407.145222
- Balakrishnan, M., Draghis, P. A., Miller, J. M., et al. 2023, *ApJ*, 947, 38, doi: 10.3847/1538-4357/acc1c9

- Baldi, A., Ettori, S., Molendi, S., et al. 2012, *A&A*, 537, A142, doi: [10.1051/0004-6361/201117836](https://doi.org/10.1051/0004-6361/201117836)
- Barrena, R., Boschin, W., Girardi, M., & Spolaor, M. 2007, *A&A*, 469, 861, doi: [10.1051/0004-6361:20077407](https://doi.org/10.1051/0004-6361:20077407)
- Belczynski, K., & Taam, R. E. 2008, *ApJ*, 685, 400, doi: [10.1086/590551](https://doi.org/10.1086/590551)
- Bell, E. F., McIntosh, D. H., Katz, N., & Weinberg, M. D. 2003, *ApJS*, 149, 289, doi: [10.1086/378847](https://doi.org/10.1086/378847)
- Biffi, V., Mernier, F., & Medvedev, P. 2018, *SSRv*, 214, 123, doi: [10.1007/s11214-018-0557-7](https://doi.org/10.1007/s11214-018-0557-7)
- Biffi, V., Rasia, E., Borgani, S., et al. 2025, *A&A*, 698, A238, doi: [10.1051/0004-6361/202453015](https://doi.org/10.1051/0004-6361/202453015)
- Biffi, V., Planelles, S., Borgani, S., et al. 2017, *MNRAS*, 468, 531, doi: [10.1093/mnras/stx444](https://doi.org/10.1093/mnras/stx444)
- Blackwell, A. E., & Bregman, J. N. 2025, *ApJ*, 979, 74, doi: [10.3847/1538-4357/ad9826](https://doi.org/10.3847/1538-4357/ad9826)
- Blackwell, A. E., Bregman, J. N., & Snowden, S. L. 2022, *ApJ*, 927, 104, doi: [10.3847/1538-4357/ac4dfb](https://doi.org/10.3847/1538-4357/ac4dfb)
- Blundell, K. M., Bowler, M. G., & Schmidtobreick, L. 2008, *ApJL*, 678, L47, doi: [10.1086/588027](https://doi.org/10.1086/588027)
- Bregman, J. N., Anderson, M. E., & Dai, X. 2010, *ApJL*, 716, L63, doi: [10.1088/2041-8205/716/1/L63](https://doi.org/10.1088/2041-8205/716/1/L63)
- Chabrier, G. 2003, *PASP*, 115, 763, doi: [10.1086/376392](https://doi.org/10.1086/376392)
- Cummings, J. D., Kalirai, J. S., Tremblay, P. E., Ramirez-Ruiz, E., & Choi, J. 2018, *ApJ*, 866, 21, doi: [10.3847/1538-4357/aadfd6](https://doi.org/10.3847/1538-4357/aadfd6)
- Dahlen, T., Strolger, L.-G., Riess, A. G., et al. 2012, *ApJ*, 757, 70, doi: [10.1088/0004-637X/757/1/70](https://doi.org/10.1088/0004-637X/757/1/70)
- De Grandi, S., Ettori, S., Longhetti, M., & Molendi, S. 2004, *A&A*, 419, 7, doi: [10.1051/0004-6361:20034228](https://doi.org/10.1051/0004-6361:20034228)
- de Plaa, J., Kaastra, J. S., Werner, N., et al. 2017, *A&A*, 607, A98, doi: [10.1051/0004-6361/201629926](https://doi.org/10.1051/0004-6361/201629926)
- Eckert, D., Gaspari, M., Gastaldello, F., Le Brun, A. M. C., & O'Sullivan, E. 2021, *Universe*, 7, 142, doi: [10.3390/universe7050142](https://doi.org/10.3390/universe7050142)
- Elbaz, D., Arnaud, M., & Vangioni-Flam, E. 1995, *A&A*, 303, 345. <https://arxiv.org/abs/astro-ph/9505107>
- Ettori, S., Morandi, A., Tozzi, P., et al. 2009, *A&A*, 501, 61, doi: [10.1051/0004-6361/200810878](https://doi.org/10.1051/0004-6361/200810878)
- Freundlich, J., & Maoz, D. 2021, *MNRAS*, 502, 5882, doi: [10.1093/mnras/stab493](https://doi.org/10.1093/mnras/stab493)
- Fryer, C. L. 1999, *ApJ*, 522, 413, doi: [10.1086/307647](https://doi.org/10.1086/307647)
- Gatuzz, E., Sanders, J. S., Dennerl, K., et al. 2023a, *MNRAS*, 526, 396, doi: [10.1093/mnras/stad2796](https://doi.org/10.1093/mnras/stad2796)
- . 2023b, *MNRAS*, 525, 6394, doi: [10.1093/mnras/stad2716](https://doi.org/10.1093/mnras/stad2716)
- Ghizzardi, S., Molendi, S., van der Burg, R., et al. 2020, *arXiv e-prints*, [arXiv:2007.01084](https://arxiv.org/abs/2007.01084), <https://arxiv.org/abs/2007.01084>
- Heger, A., & Woosley, S. E. 2002, *ApJ*, 567, 532, doi: [10.1086/338487](https://doi.org/10.1086/338487)
- Kim, D.-W., Anderson, C., Burke, D., et al. 2018, *ApJ*, 853, 129, doi: [10.3847/1538-4357/aaa43a](https://doi.org/10.3847/1538-4357/aaa43a)
- Kim, M., Jee, M. J., Finner, K., et al. 2019, *ApJ*, 874, 143, doi: [10.3847/1538-4357/ab0d7c](https://doi.org/10.3847/1538-4357/ab0d7c)
- Kobayashi, C., Umeda, H., Nomoto, K., Tominaga, N., & Ohkubo, T. 2006, *ApJ*, 653, 1145, doi: [10.1086/508914](https://doi.org/10.1086/508914)
- Kravtsov, A. V., & Borgani, S. 2012a, *ARA&A*, 50, 353, doi: [10.1146/annurev-astro-081811-125502](https://doi.org/10.1146/annurev-astro-081811-125502)
- . 2012b, *ARA&A*, 50, 353, doi: [10.1146/annurev-astro-081811-125502](https://doi.org/10.1146/annurev-astro-081811-125502)
- Kravtsov, A. V., Vikhlinin, A., & Nagai, D. 2006, *ApJ*, 650, 128, doi: [10.1086/506319](https://doi.org/10.1086/506319)
- Kroupa, P. 2001, *MNRAS*, 322, 231, doi: [10.1046/j.1365-8711.2001.04022.x](https://doi.org/10.1046/j.1365-8711.2001.04022.x)
- Kudritzki, R.-P., Ho, I.-T., Schrubba, A., et al. 2015, *MNRAS*, 450, 342, doi: [10.1093/mnras/stv522](https://doi.org/10.1093/mnras/stv522)
- Laganá, T. F., Lovisari, L., Martins, L., et al. 2015, *A&A*, 573, A66, doi: [10.1051/0004-6361/201424821](https://doi.org/10.1051/0004-6361/201424821)
- Laganá, T. F., Martinet, N., Durret, F., et al. 2013, *A&A*, 555, A66, doi: [10.1051/0004-6361/201220423](https://doi.org/10.1051/0004-6361/201220423)
- Lau, E. T., Kravtsov, A. V., & Nagai, D. 2009, *ApJ*, 705, 1129, doi: [10.1088/0004-637X/705/2/1129](https://doi.org/10.1088/0004-637X/705/2/1129)
- Lima Neto, G. B., Capelato, H. V., Durret, F., & Machado, R. E. G. 2025, *A&A*, 697, A185, doi: [10.1051/0004-6361/202453614](https://doi.org/10.1051/0004-6361/202453614)
- Lima Neto, G. B., Capelato, H. V., Sodré, Jr., L., & Proust, D. 2003, *A&A*, 398, 31, doi: [10.1051/0004-6361:20021656](https://doi.org/10.1051/0004-6361:20021656)
- Loewenstein, M. 2001, *ApJ*, 557, 573, doi: [10.1086/322256](https://doi.org/10.1086/322256)
- . 2013, *ApJ*, 773, 52, doi: [10.1088/0004-637X/773/1/52](https://doi.org/10.1088/0004-637X/773/1/52)
- Lovisari, L., & Reiprich, T. H. 2019, *MNRAS*, 483, 540, doi: [10.1093/mnras/sty3130](https://doi.org/10.1093/mnras/sty3130)
- Lovisari, L., Reiprich, T. H., & Schellenberger, G. 2015, *A&A*, 573, A118, doi: [10.1051/0004-6361/201423954](https://doi.org/10.1051/0004-6361/201423954)
- Lovisari, L., Schellenberger, G., Sereno, M., et al. 2020, *ApJ*, 892, 102, doi: [10.3847/1538-4357/ab7997](https://doi.org/10.3847/1538-4357/ab7997)
- Ma, X., Wang, X., Mo, J., et al. 2025, *arXiv e-prints*, [arXiv:2504.04393](https://arxiv.org/abs/2504.04393), doi: [10.48550/arXiv.2504.04393](https://doi.org/10.48550/arXiv.2504.04393)
- Madau, P., & Dickinson, M. 2014, *ARA&A*, 52, 415, doi: [10.1146/annurev-astro-081811-125615](https://doi.org/10.1146/annurev-astro-081811-125615)
- Mantz, A. B., Allen, S. W., Morris, R. G., et al. 2017, *MNRAS*, 472, 2877, doi: [10.1093/mnras/stx2200](https://doi.org/10.1093/mnras/stx2200)
- Maughan, B. J., Jones, C., Forman, W., & Van Speybroeck, L. 2008, *ApJS*, 174, 117, doi: [10.1086/521225](https://doi.org/10.1086/521225)
- McCarthy, I. G., Schaye, J., Ponman, T. J., et al. 2010, *MNRAS*, 406, 822, doi: [10.1111/j.1365-2966.2010.16750.x](https://doi.org/10.1111/j.1365-2966.2010.16750.x)
- Mernier, F., de Plaa, J., Kaastra, J. S., et al. 2017, *A&A*, 603, A80, doi: [10.1051/0004-6361/201630075](https://doi.org/10.1051/0004-6361/201630075)

- Molendi, S., Eckert, D., De Grandi, S., et al. 2016, *A&A*, 586, A32, doi: [10.1051/0004-6361/201527356](https://doi.org/10.1051/0004-6361/201527356)
- Mulchaey, J. S., & Zabludoff, A. I. 1999, *ApJ*, 514, 133, doi: [10.1086/306952](https://doi.org/10.1086/306952)
- Nelson, D., Pillepich, A., Ayromlou, M., et al. 2024, *A&A*, 686, A157, doi: [10.1051/0004-6361/202348608](https://doi.org/10.1051/0004-6361/202348608)
- Nomoto, K., Kobayashi, C., & Tominaga, N. 2013, *ARA&A*, 51, 457, doi: [10.1146/annurev-astro-082812-140956](https://doi.org/10.1146/annurev-astro-082812-140956)
- Paul, S., John, R. S., Gupta, P., & Kumar, H. 2017, *MNRAS*, 471, 2, doi: [10.1093/mnras/stx1488](https://doi.org/10.1093/mnras/stx1488)
- Pipino, A., Matteucci, F., Borgani, S., & Biviano, A. 2002, *NewA*, 7, 227, doi: [10.1016/S1384-1076\(02\)00136-7](https://doi.org/10.1016/S1384-1076(02)00136-7)
- Planck Collaboration, Aghanim, N., Akrami, Y., et al. 2018, arXiv e-prints, arXiv:1807.06209. <https://arxiv.org/abs/1807.06209>
- Pratt, G. W., Arnaud, M., Biviano, A., et al. 2019, *SSRv*, 215, 25, doi: [10.1007/s11214-019-0591-0](https://doi.org/10.1007/s11214-019-0591-0)
- Raghavan, D., McAlister, H. A., Henry, T. J., et al. 2010, *ApJS*, 190, 1, doi: [10.1088/0067-0049/190/1/1](https://doi.org/10.1088/0067-0049/190/1/1)
- Randall, S. W., Jones, C., Markevitch, M., et al. 2009, *ApJ*, 700, 1404, doi: [10.1088/0004-637X/700/2/1404](https://doi.org/10.1088/0004-637X/700/2/1404)
- Rasia, E., Borgani, S., Murante, G., et al. 2015, *ApJL*, 813, L17, doi: [10.1088/2041-8205/813/1/L17](https://doi.org/10.1088/2041-8205/813/1/L17)
- Renzini, A., & Andreon, S. 2014, *MNRAS*, 444, 3581, doi: [10.1093/mnras/stu1689](https://doi.org/10.1093/mnras/stu1689)
- Roper, F. A., Cai, Y.-C., & Peacock, J. A. 2025, arXiv e-prints, arXiv:2510.12553, doi: [10.48550/arXiv.2510.12553](https://doi.org/10.48550/arXiv.2510.12553)
- Russell, P. A., Ponman, T. J., & Sanderson, A. J. R. 2007, *MNRAS*, 378, 1217, doi: [10.1111/j.1365-2966.2007.11660.x](https://doi.org/10.1111/j.1365-2966.2007.11660.x)
- Sharma, S. 2017, *ARA&A*, 55, 213, doi: [10.1146/annurev-astro-082214-122339](https://doi.org/10.1146/annurev-astro-082214-122339)
- Simionescu, A., Nakashima, S., Yamaguchi, H., et al. 2019, *MNRAS*, 483, 1701, doi: [10.1093/mnras/sty3220](https://doi.org/10.1093/mnras/sty3220)
- Sivanandam, S., Zabludoff, A. I., Zaritsky, D., Gonzalez, A. H., & Kelson, D. D. 2009, *ApJ*, 691, 1787, doi: [10.1088/0004-637X/691/2/1787](https://doi.org/10.1088/0004-637X/691/2/1787)
- Snowden, S. L., Mushotzky, R. F., Kuntz, K. D., & Davis, D. S. 2008, *A&A*, 478, 615, doi: [10.1051/0004-6361:20077930](https://doi.org/10.1051/0004-6361:20077930)
- Tornatore, L., Borgani, S., Dolag, K., & Matteucci, F. 2007, *MNRAS*, 382, 1050, doi: [10.1111/j.1365-2966.2007.12070.x](https://doi.org/10.1111/j.1365-2966.2007.12070.x)
- Vikhlinin, A., Kravtsov, A., Forman, W., et al. 2006, *ApJ*, 640, 691, doi: [10.1086/500288](https://doi.org/10.1086/500288)
- Werner, N., Durret, F., Ohashi, T., Schindler, S., & Wiersma, R. P. C. 2008, *SSRv*, 134, 337, doi: [10.1007/s11214-008-9320-9](https://doi.org/10.1007/s11214-008-9320-9)
- Wu, H.-Y., Evrard, A. E., Hahn, O., et al. 2015, *MNRAS*, 452, 1982, doi: [10.1093/mnras/stv1434](https://doi.org/10.1093/mnras/stv1434)
- Young, O. E., Thomas, P. A., Short, C. J., & Pearce, F. 2011, *MNRAS*, 413, 691, doi: [10.1111/j.1365-2966.2010.18165.x](https://doi.org/10.1111/j.1365-2966.2010.18165.x)
- Zibetti, S., White, S. D. M., Schneider, D. P., & Brinkmann, J. 2005, *MNRAS*, 358, 949, doi: [10.1111/j.1365-2966.2005.08817.x](https://doi.org/10.1111/j.1365-2966.2005.08817.x)

Table 1. Total Data Set

Cluster	RA	Dec	z	R_{500} (kpc)	$M_{gas,500}$ (M_{\odot})	M_*/M_{gas}	Z_{ICM} (Z_{\odot})
NGC1132	02h52m51.9s	-01d16m29s	0.023	383.5	$(1.24 \pm 0.03) \times 10^{12}$	0.48 ± 0.09	0.24 ± 0.02
A586	07h32m20.160s	+31d37m55.92s	0.17	1265.8	$(6.9 \pm 0.06) \times 10^{13}$	0.43 ± 0.10	0.44 ± 0.05
NGC5098	13h20m16.2s	+33d08m39s	0.037	344.6	$(1.3 \pm 0.21) \times 10^{12}$	0.42 ± 0.13	0.15 ± 0.01
RXCJ2315.7-0222	23h15m44.1s	-02d22m59s	0.027	427.1	$(1.86 \pm 0.19) \times 10^{12}$	0.38 ± 0.10	0.46 ± 0.03
NGC4104	12h06m39.0s	+28d10m27s	0.028	502.5	$(2.05 \pm 0.09) \times 10^{12}$	0.34 ± 0.09	0.44 ± 0.08
A2259	17h20m10.080s	+27d39m03.28s	0.16	1117.1	$(5.5 \pm 0.4) \times 10^{13}$	0.27 ± 0.08	0.36 ± 0.03
A2034	15h10m12.480s	+33d30m28.08s	0.11	1315.5	$(7.3 \pm 0.2) \times 10^{13}$	0.23 ± 0.07	0.38 ± 0.07
MS0906.5+1110	09h09m12.720s	+10d48m32.88s	0.18	923.0	$(4.4 \pm 0.2) \times 10^{13}$	0.21 ± 0.07	0.37 ± 0.04
NGC4325	12h33m06.7s	+10d37m16s	0.026	408.6	$(1.50 \pm 0.02) \times 10^{12}$	0.19 ± 0.05	0.21 ± 0.02
A1991	14h54m30.2s	+18d37m51s	0.059	563.3	$(6.68 \pm 0.12) \times 10^{12}$	0.16 ± 0.05	0.38 ± 0.03
A383	02h48m03.432s	-03d31m45.87s	0.19	971.2	$(4.0 \pm 0.2) \times 10^{13}$	0.12 ± 0.04	0.48 ± 0.06
AWM4	16h04m57.0s	+23d55m14s	0.032	547.8	$(5.60 \pm 0.29) \times 10^{12}$	0.11 ± 0.03	0.44 ± 0.05
A267	01h52m42.144s	+01d00m41.29s	0.23	953.3	$(5.2 \pm 0.5) \times 10^{13}$	0.11 ± 0.03	0.49 ± 0.07
A1689	13h11m29.520s	-01d20m29.68s	0.18	1487.5	$(12.0 \pm 0.5) \times 10^{13}$	0.098 ± 0.029	0.44 ± 0.04
A2261	17h22m27.120s	+32d07m56.28s	0.22	1176.8	$(9.7 \pm 0.4) \times 10^{13}$	0.095 ± 0.029	0.37 ± 0.05
A781	09h20m26.160s	+30d30m02.52s	0.30	984.4	$(6.6 \pm 0.5) \times 10^{13}$	0.091 ± 0.028	0.37 ± 0.05
A1413	11h55m18.000s	+23d24m17.28s	0.14	1330.7	$(8.4 \pm 0.3) \times 10^{13}$	0.088 ± 0.026	0.46 ± 0.05
A773	09h17m53.040s	+51d43m39.72s	0.22	1306.3	$(9.6 \pm 0.4) \times 10^{13}$	0.083 ± 0.025	0.35 ± 0.06
RXJ1720.1+2638	17h20m16.800s	+26d38m06.60s	0.39	1178.4	$(7.3 \pm 0.4) \times 10^{13}$	0.077 ± 0.024	0.53 ± 0.04
A2409	22h00m52.800s	+20d58m27.84s	0.15	1177.1	$(6.4 \pm 0.4) \times 10^{13}$	0.073 ± 0.022	0.47 ± 0.04
A1914	14h26m00.960s	+37m49d33.96s	0.17	1503.5	$(11.7 \pm 0.7) \times 10^{13}$	0.069 ± 0.021	0.28 ± 0.04
A1763	13h35m18.240s	+40d59m59.28s	0.22	1328.3	$(11.5 \pm 0.6) \times 10^{13}$	0.069 ± 0.021	0.39 ± 0.06
MS1455.0+2232	14h57m15.120s	+22d20m35.52s	0.26	930.3	$(5.0 \pm 0.2) \times 10^{13}$	0.066 ± 0.020	0.42 ± 0.05
A665	08h30m57.360s	+65d50m33.36s	0.18	1357.3	$(12.6 \pm 0.5) \times 10^{13}$	0.046 ± 0.014	0.37 ± 0.11
A697	08h42m57.600s	+36d21m55.80s	0.28	1455.7	$(16.1 \pm 1.1) \times 10^{13}$	0.044 ± 0.013	0.31 ± 0.05
A2069	15h24m39.849s	+29d53m26.33s	0.12	1173.2	$(6.3 \pm 0.3) \times 10^{13}$	0.040 ± 0.010	0.30 ± 0.04

Table 2. kT (keV)

Cluster	obs ID	$< 0.1R_{500}$	$0.1 - 0.21R_{500}$	$0.21 - 0.39R_{500}$	$0.39 - 0.53R_{500}$	$0.53 - 0.7R_{500}$
NGC1132	0151490101	1.184 ± 0.010	1.146 ± 0.094	1.189 ± 0.011	1.103 ± 0.022	1.047 ± 0.040
A586	827051101	6.584 ± 0.185	11.284 ± 0.795	6.445 ± 0.216	7.694 ± 0.690	3.942 ± 0.450
	0673850201	7.107 ± 0.264	6.927 ± 0.278	4.879 ± 0.243	5.837 ± 0.594	5.293 ± 1.439
NGC5098	0105860101	1.023 ± 0.006	1.205 ± 0.011	1.233 ± 0.017	1.069 ± 0.019	0.956 ± 0.024
RXCJ 2315.7-0222	501110101	1.560 ± 0.015	1.761 ± 0.027	1.651 ± 0.030	1.496 ± 0.040	1.536 ± 0.066
NGC4104	0301900401	1.496 ± 0.033	2.334 ± 0.114	2.000 ± 0.106	1.823 ± 0.211	2.639 ± 0.746
A2259	0827040101	5.980 ± 0.165	5.731 ± 0.120	4.963 ± 0.145	5.091 ± 0.191	4.931 ± 0.386
A2034	149880101	4.772 ± 0.214	6.279 ± 0.240	6.584 ± 0.331	7.175 ± 0.778	6.435 ± 1.091
	303930101	7.322 ± 0.304	7.399 ± 0.346	7.747 ± 0.453	4.575 ± 0.444	6.298 ± 1.587
MS0906.5+1110	673850901	6.435 ± 0.468	5.635 ± 0.363	5.632 ± 0.249	5.460 ± 0.408	
	827351301	6.632 ± 0.527	5.971 ± 0.348	5.328 ± 0.279	5.637 ± 0.230	5.283 ± 0.563
NGC4325	0108860101	0.959 ± 0.003	1.099 ± 0.007	1.052 ± 0.010	0.979 ± 0.018	0.929 ± 0.041
A1991	0145020101	1.805 ± 0.013	2.953 ± 0.066	2.558 ± 0.515	2.174 ± 0.088	2.037 ± 0.151
A383	0084230501	3.463 ± 0.058	4.726 ± 0.117	4.837 ± 0.142	4.580 ± 0.260	4.588 ± 0.430
AWM4	0093060401	2.490 ± 0.041	2.504 ± 0.049	2.016 ± 0.072	2.710 ± 0.190	1.849 ± 0.178
A267	0084230401	6.629 ± 0.059	$5.936 \text{ pm } 0.298$	5.801 ± 0.270	5	5.109 ± 0.444
A1689	0093030101	8.864 ± 0.144	8.490 ± 0.188	8.835 ± 0.019	9.275 ± 0.432	
A2261	6931809101	7.362 ± 0.218	7.869 ± 0.211	8.156 ± 0.357	7.833 ± 0.414	6.078 ± 0.328
A781	0401170101	5.913 ± 1.518	6.264 ± 0.558	5.241 ± 0.218	6.813 ± 0.427	5.592 ± 0.276
A1413	0502690101	7.204 ± 0.131	6.728 ± 0.147	7.059 ± 0.159	6.730 ± 0.274	6.912 ± 0.582
	0502690201	7.151 ± 0.086	7.450 ± 0.113	7.352 ± 0.115	7.413 ± 0.235	7.606 ± 0.288
	0551280101	7.255 ± 0.098	7.100 ± 0.107	7.445 ± 0.128	7.178 ± 0.225	7.028 ± 0.373
	0551280201	7.173 ± 0.096	7.483 ± 0.134	7.001 ± 0.117	7.020 ± 0.223	6.506 ± 0.367

Table 3. Table 2 cot.

Cluster	obs ID	$< 0.1R_{500}$	$0.1 - 0.21R_{500}$	$0.21 - 0.39R_{500}$	$0.39 - 0.53R_{500}$	$0.53 - 0.7R_{500}$
A773	0084230601	9.694 ± 0.869	7.865 ± 0.298	7.797 ± 0.270	7.352 ± 0.524	8.256 ± 0.833
RXJ1720.1+2638	0500670201	4.194 ± 0.095	6.763 ± 0.165	6.760 ± 0.275	8.119 ± 0.612	6.5
	0500670301	4.908 ± 0.065	6.727 ± 0.149	7.389 ± 0.229	6.670 ± 0.354	6.640 ± 0.565
	0500670401	5.018 ± 0.081	6.864 ± 0.202	6.652 ± 0.237	6.893 ± 0.472	6.5
A2409	0827020101	9.694 ± 0.869	5.888 ± 0.156	6.100 ± 0.151	5.551 ± 0.236	6.541 ± 0.555
A1914	0112230201	6.664 ± 0.159	5.586 ± 0.149	6.209 ± 0.234	7.465 ± 0.440	7.292 ± 0.610
A1763	0084230901	6.196 ± 0.473	6.040 ± 0.306	5.660 ± 0.237	5.582 ± 0.354	4.532 ± 0.284
MS1455+2232	0108670201	3.959 ± 0.063	4.717 ± 0.092	5.050 ± 0.133	5.385 ± 0.246	4.420 ± 0.285
A665	0109890401	6.938 ± 0.721	6.949 ± 0.551	7.048 ± 0.514	7.396 ± 0.814	6.801 ± 0.957
A697	0827041001	10.334 ± 0.700	8.787 ± 0.409	9.938 ± 0.357	9.233 ± 0.522	8.388 ± 0.644
A2069	0827010601	6.178 ± 0.323	7.023 ± 0.259	5.993 ± 0.160	9.008 ± 0.473	6.194 ± 0.451

Table 4. $Z_{ICM}(Z_{\odot})$

Cluster	obs ID	$< 0.1R_{500}$	$0.1 - 0.21R_{500}$	$0.21 - 0.39R_{500}$	$0.39 - 0.53R_{500}$	$0.53 - 0.7R_{500}$
NGC1132	0151490101	0.564 ± 0.045	0.330 ± 0.022	0.297 ± 0.021	0.183 ± 0.026	0.144 ± 0.040
A586	827051101	0.620 ± 0.063	0.235 ± 0.129	0.534 ± 0.076	0.600 ± 0.196	0.127 ± 0.159
	0673850201	0.524 ± 0.083	0.421 ± 0.078	0.411 ± 0.079	0.231 ± 0.213	0.527 ± 0.707
NGC5098	0105860101	0.362 ± 0.021	0.395 ± 0.031	0.248 ± 0.021	0.155 ± 0.020	0.090 ± 0.017
RXCJ 2315.7-0222	501110101	0.791 ± 0.041	0.645 ± 0.043	0.495 ± 0.037	0.377 ± 0.050	1.589 ± 0.656
NGC4104	0301900401	0.228 ± 0.026	0.458 ± 0.083	0.425 ± 0.083	0.482 ± 0.206	0.748 ± 0.604
A2259	0827040101	0.508 ± 0.063	0.442 ± 0.045	0.364 ± 0.036	0.404 ± 0.085	0.247 ± 0.130
A2034	149880101	0.360 ± 0.073	0.530 ± 0.076	0.391 ± 0.097	0.451 ± 0.247	1.786 ± 0.0896
	303930101	0.400 ± 0.079	0.465 ± 0.072	0.399 ± 0.113	$7e-4, \pm 0.258$	0.626 ± 0.602
MS0906.5+1110	673850901	0.753 ± 0.203	0.456 ± 0.119	0.539 ± 0.108	0.119 ± 0.177	
	827351301	0.437 ± 0.156	0.546 ± 0.104	0.340 ± 0.075	0.363 ± 0.076	0.296 ± 0.195
NGC4325	0108860101	0.558 ± 0.021	0.441 ± 0.025	0.282 ± 0.023	0.229 ± 0.038	0.087 ± 0.027
A1991	0145020101	0.651 ± 0.023	0.831 ± 0.059	0.472 ± 0.039	0.262 ± 0.045	0.338 ± 0.100
A383	0084230501	0.857 ± 0.057	0.626 ± 0.065	0.551 ± 0.069	0.315 ± 0.108	0.495 ± 0.217
AWM4	0093060401	0.740 ± 0.047	0.550 ± 0.041	0.409 ± 0.056	0.532 ± 0.124	0.862 ± 0.321
A267	0084230401	0.493 ± 0.192	0.589 ± 0.113	0.490 ± 0.093	0.451 ± 0.145	0.546 ± 0.222
A1689	0093030101	0.501 ± 0.032	0.358 ± 0.034	0.475 ± 0.042	0.290 ± 0.080	
A2261	6931809101	0.630 ± 0.065	0.534 ± 0.054	0.293 ± 0.072	0.504 ± 0.104	0.382 ± 0.104
A781	0401170101	0.508 ± 0.552	0.345 ± 0.164	0.397 ± 0.083	0.316 ± 0.119	0.372 ± 0.092
A1413	0502690101	0.638 ± 0.043	0.437 ± 0.041	0.472 ± 0.046	0.522 ± 0.090	0.034 ± 0.135
	0502690201	0.588 ± 0.028	0.467 ± 0.031	0.427 ± 0.029	0.421 ± 0.060	0.407 ± 0.079
	0551280101	0.649 ± 0.030	0.528 ± 0.033	0.527 ± 0.036	0.389 ± 0.063	0.478 ± 0.108
	0551280201	0.571 ± 0.030	0.416 ± 0.035	0.481 ± 0.034	0.460 ± 0.066	0.434 ± 0.106

Table 5. Table 4 cont.

Cluster	obs ID	$< 0.1R_{500}$	$0.1 - 0.21R_{500}$	$0.21 - 0.39R_{500}$	$0.39 - 0.53R_{500}$	$0.53 - 0.7R_{500}$
A773	0084230601	0.323 ± 0.159	0.516 ± 0.101	0.367 ± 0.081	0.307 ± 0.129	0.358 ± 0.183
RXJ1720.1+2638	0500670201	0.797 ± 0.085	0.516 ± 0.065	0.401 ± 0.087	0.676 ± 0.212	0.418 ± 0.274
	0500670301	0.734 ± 0.036	0.557 ± 0.049	0.470 ± 0.067	0.512 ± 0.114	0.589 ± 0.193
	0500670401	0.763 ± 0.047	0.572 ± 0.065	0.712 ± 0.089	0.593 ± 0.159	0.834 ± 0.239
A2409	0827020101	0.323 ± 0.159	0.566 ± 0.061	0.466 ± 0.052	0.566 ± 0.097	0.284 ± 0.152
A1914	0112230201	0.372 ± 0.043	0.204 ± 0.031	0.238 ± 0.046	0.314 ± 0.103	0.781 ± 0.189
A1763	0084230901	0.624 ± 0.177	0.545 ± 0.109	0.367 ± 0.079	0.481 ± 0.132	0.381 ± 0.144
MS1455+2232	0108670201	0.625 ± 0.044	0.527 ± 0.046	0.428 ± 0.057	0.462 ± 0.103	0.291 ± 0.146
A665	0109890401	0.188 ± 0.176	0.483 ± 0.154	0.417 ± 0.139	0.373 ± 0.243	0.220 ± 0.252
A697	0827041001	0.478 ± 0.130	0.386 ± 0.075	0.359 ± 0.069	0.365 ± 0.110	0.069 ± 0.130
A2069	0827010601	0.503 ± 0.113	0.419 ± 0.071	0.392 ± 0.053	0.128 ± 0.084	0.163 ± 0.112